Journal of Nuclear Materials 429 (2012) 353–367

Contents lists available at SciVerse ScienceDirect

Journal of Nuclear Materials

journal homepage: www.elsevier.com/locate/jnucmat

The effects of γ-radiation on model vitreous wasteforms intended for the disposal of intermediate and high level radioactive wastes in the United Kingdom

O.J. McGann [a], P.A. Bingham [a], R.J. Hand [a], A.S. Gandy [a], M. Kavčič [b], M. Žitnik [b], K. Bučar [b], R. Edge [c], N.C. Hyatt [a,*]

[a] Immobilisation Science Laboratory, Department of Materials Science and Engineering, University of Sheffield, Sir Robert Hadfield Building, Mappin Street, Sheffield S1 3JD, UK
[b] J. Stefan Institute, Jamova 39, SI-1000 Ljubljana, Slovenia
[c] Dalton Cumbrian Facility, University of Manchester, Westlakes Science and Technology Park, Moor Row, Cumbria CA24 3HA, UK

ARTICLE INFO

Article history:
Received 5 February 2012
Accepted 10 April 2012
Available online 21 April 2012

ABSTRACT

The effect of γ-radiation on a variety of model vitreous wasteforms applied to, or conceived for, immobilisation of UK intermediate and high level radioactive wastes was studied up to a dose of 8 MGy. It was determined that γ-irradiation up to this dose had no significant effect upon the mechanical properties of the wasteforms and there was no evidence of residual structural defects. FTIR and Raman spectroscopy showed no evidence of radiation directly affecting the silicate network of the glasses. The negligible impact of this γ-irradiation dose on the physical properties of the glass was attributed to the presence of multivalent ions, particularly Fe, and a mechanism by which the electron–hole pairs generated by γ-irradiation were annihilated by the Fe^{2+}–Fe^{3+} redox mechanism. However, reduction of sulphur species in response to γ-radiation was demonstrated by S K-edge XANES and XES data.

1. Introduction and background

Vitrification is the currently accepted technology for the immobilisation of the high level radioactive wastes arising from the reprocessing of nuclear fuels and has been deployed on an industrial scale since at least 1977 [1]. Radioactive waste vitrification has been applied by the USA, UK, Russia, France and Germany [2–4], and to date has been used in the production of at least 11,000 canisters of vitrified waste [5]. The purpose of these vitrified wasteforms is to function as the primary barrier to the release of radionuclides to the environment, within a multi-barrier geological disposal facility. A vitrified wasteform must therefore be expected to withstand a range of adverse conditions over periods of 10^2–10^6 years, with a minimal and quantifiable deterioration in chemical or mechanical integrity which could result in the release of radionuclides to the environment [6–8].

The decay of fission products and actinides in radioactive waste glasses results in the emission of ionising radiation which may interact with the vitreous material through several mechanisms, potentially leading to an adverse impact on the long term physical and chemical stability of the material [9,10]. Ionising radiation has been linked to changes in the coordination environment of the species comprising the glass network in alkali-borosilicate glasses, which typically results in a small increase in density, with a concomitant effect on mechanical properties [11]. The interaction of ionising radiation with alkali-borosilicate glasses has also been linked to the formation of oxygen bubbles, the formation of various defect centres [11], and, at very high radiation doses, even phase separation [12]. Such γ-radiation induced changes in structure and constitution may adversely affect the long term mechanical integrity and chemical durability of the wasteform [12]. These ionisation interactions are commonly associated with β- and γ-radiation; α-particles and neutrons typically interact with glasses through ballistic processes which result in atomic displacements [11]. As such, these ballistic processes result in stronger effects at equivalent doses, and can even produce cracking and crazing in glasses, as well as significant densification [11], however, these effects are not generally observed in response to γ-radiation.

β-Decay of fission products leads to the emission of γ-ray photons which interact with the glass matrix primarily through Compton Scattering and the photoelectric effect [9]. Absorption of γ-ray photons results in the formation of mobile electron and hole pairs which can lead to metastable defects associated with a change in element valence state and coordination. These effects are comparable to some extent with the effects of electron irradiation [13]. Furthermore, since γ-radiation is more penetrating than other forms of ionising radiation, its effects typically permeate the entirety of a glass wasteform instead of being limited to structural regions local to the radiation source. The impact of γ-irradiation on the properties of a glass can be diverse and depends heavily upon the composition of the glass in question. Experiments involving ion

* Corresponding author. Tel.: +44 114 2225470.
E-mail address: n.c.hyatt@sheffield.ac.uk (N.C. Hyatt).

0022-3115/$ - see front matter © 2012 Elsevier B.V. All rights reserved.
http://dx.doi.org/10.1016/j.jnucmat.2012.04.007

beam irradiation of amorphous silica revealed that ionising radiation resulted in the formation of crystalline regions and overall increase in density, as result of bond modification in the amorphous silica network [14]. These effects were also noted to be strongly dependent upon the precise chemical composition [15].

In borosilicate glass compositions, similar to those used for radioactive waste vitrification, it was observed that γ-radiation induced the formation of boron-oxygen hole centre (BOHC) defect sites, which were detectable by electron paramagnetic resonance (EPR) spectroscopy [16]. However, the impact of γ-irradiation is not limited to defect formation and, typically, in borosilicate glasses, a range of effects have been reported to occur: the formation of colour centres occurs at low doses of γ-radiation (0.018 MGy) [18]; and at higher doses (>1 MGy) an increase in silicate network polymerisation and decrease in average Si–O–Si bond angle, leading to an increase in glass density and mechanical strength [17,19]. γ-Radiation might therefore be expected to cause a range of detectable effects in borosilicate glasses due to the induced defects and changes in bonding of the borate and silicate networks caused by electron and hole pairs.

Research has demonstrated that the presence of transition metal species in silicate glasses, such as Fe, Cr, Zr, and some actinides such as U, may inhibit the accumulation of β-radiation induced defects, similar to those noted above [15,16]. The mechanism of this effect, proposed by Debnath [20], is linked to the ability of these elements to effectively 'trap' the excitons (electron and hole pairs) produced by ionising radiation *via* changes in oxidation states, such as the ferrous and ferric oxidation states of iron [13]. As the different oxidation states of these elements usually coexist in oxide glasses, the excitons produced by the incident radiation are prevented from forming structural defects because they are removed from the system by the coupled redox changes of these elements [13]. Whilst the effects of electron beam and β-radiation cannot be directly compared to the effects of γ-radiation, due to the difference in energy loss mechanisms, qualitative comparison between mechanisms which inhibit radiation damage may be useful. Indeed, it has been shown that in the case of γ-irradiation of iron containing glasses, iron redox can act to trap electron and hole pairs, depending on iron content and on radiation dose [9,20].

The aim of the current study was to investigate the effect of γ-radiation on a variety of model vitreous wasteforms applied to, or conceived for, immobilisation of UK intermediate and high level radioactive wastes, up to a dose of 8 MGy.

2. Experimental procedures

Irradiation experiments employed a selection of glass compositions which are either in consideration for use in the vitrification UK ILW (Intermediate Level Wastes), namely glasses G11, G73 and G78, or are already used for UK HLW (High Level Waste vitrification), namely glass MW-25%. All of the glasses were loaded with appropriate inactive simulated wastes. The compositions of these wasteforms and key preparation details are listed in Table 1.

Glasses G11 and G78 are similar to several of the mixed alkali borosilicate glasses, including the "MW" base glass developed and used for vitrification of UK HLW [22]. In contrast, glass G73 is distinct as it is an alkali–alkaline earth borosilicate. These three glass compositions were designed for ILW waste vitrification [23,24], and all contain quantities of Fe_2O_3 in their compositions for improved compatibility with the intended waste stream through control of glass redox. These three glasses were loaded with simulated ILW waste (an ion exchange resin) with high organic and sulphur contents. MW-25% is an inactive simulant UK HLW glass, the composition of this material corresponds to 25% of HLW waste oxides from spent Magnox fuel, incorporated within an alkali borosilicate (MW) base glass.

Table 1
Glass compositions (mol%) and processing temperatures (°C).

Component	G11	G73	G78	MW-25%
SiO_2	58.2	50.2	58.8	48.4
B_2O_3	9.1	2.2	17.8	17.2
Al_2O_3	2.5	0.4	–	5.1
Fe_2O_3	5.2	2.9	3.9	3.4
CaO	–	10.7	–	–
BaO	–	17.6	–	–
Li_2O	10.6	7.6	10.4	4.2
Na_2O	13.3	3.0	8.0	8.7
MgO	–	–	–	8.4
Other oxides	–	–	–	4.6
SO_3	1.1	5.4	1.1	–
Melting temperature	1200	1200	1200	1060
Annealing temperature	450	480	480	500

Glasses were melted in recrystallised alumina crucibles using an electrical muffle furnace. Melting temperatures ranged from 1060 °C to 1200 °C depending on glass composition. Glasses were melted for 2 h before pouring into a steel mould and annealed in a muffle furnace, set close to the glass transition temperature (T_g) for the glass composition. The melting and annealing temperatures are given in Table 1.

Annealed glass prisms, measuring approximately 10 mm × 10 mm × (100 − 200) mm, were subsequently exposed to a γ-radiation dose of 4 or 8 MGy, a control specimen (0 MGy) was retained for each composition. The γ-radiation source was ^{60}Co (2.824 MeV) and irradiation was carried out at the UK AEA Harwell Site.

The 8 MGy dose represents the approximate accumulated γ-dose expected for wasteforms G11, G73 and G78 over the first 8.7 years of lifetime, and the first 0.13 years of lifetime for the wasteform MW-25%. The estimates for G11, G73 and G78 are based on the γ-irradiation produced by the decay of 0.1 wt% ^{137}Cs, which is the proportion expected in the optimum 35 wt% loading of ILW simulant waste (Cs loaded, sulphonated ion exchange resin). The estimate for MW-25% is based on values published by Marples et al. for this type of wasteform (loaded with 25 wt% of an HLW simulant waste) [22]. Post-irradiation, the samples were stored in a dark and refrigerated environment (approximately −15 °C) to reduce the potential for the annealing of radiation induced defects.

A wide selection of experimental techniques was implemented to determine the effect of γ-irradiation upon the glasses, for the purpose of this communication they are divided into two broad categories: mechanical techniques and spectroscopic techniques.

2.1. Mechanical techniques

A resonant frequency technique was applied to determine the effect of γ-radiation on Young's modulus, shear modulus and Poisson's ratio. Vickers indentation, utilising a diamond tipped indenter, was applied to determine the effect of γ-radiation on glass hardness and fracture toughness.

Davis [25], demonstrated that the shear and Young's modulus of a material can be determined non-destructively by measuring the resonant frequency of an internal standing acoustic wave, generated by mechanical excitation using an electrostatic drive. The resonant frequency can be connected to the elastic constants of the material through the following equations:

$$E = 4 \times 10^{-6} f_0^2 l^2 \rho \times \left[\frac{1}{\left[1 - \frac{(\pi\nu)^2}{2l^2} \frac{(h^2+b^2)}{12} \right]^2} \right] \quad (1)$$

and

$$G = 4 \times 10^{-6} f_0^2 l^2 \rho \times \left[\frac{\left(\frac{h}{b}\right) + \left(\frac{b}{h}\right)}{4\left(\frac{h}{b}\right) - 2.52\left(\frac{h}{b}\right)^2 + 0.21\left(\frac{h}{b}\right)^6} \right] \quad (2)$$

with

$$v = \frac{E}{2G} - 1 \quad (3)$$

where E is the Young's modulus, G the shear modulus, f_0 the resonant frequency, l the length of the sample, ρ the material density, v the Poisson's ratio, h the height of the sample and b is the width of the sample; assuming the sample is a regular prism. By finding the resonant frequency of the material both in the longitudinal mode (i.e. the resonant frequency of a first order standing wave parallel to the length of a prism) and the flexural mode (i.e. the resonant frequency of a first order standing wave passing diagonally across the length of a prism) the Young's modulus and shear modulus can be experimentally determined; a comprehensive experimental description has been published elsewhere [25]. Poisson's ratio can be determined from the resulting shear and Young's modulus results (Eq. (3)).

Micro-indentation experiments were performed based upon the work of Connelly et al. [28] using a Mitutoyo HM hardness testing machine. Experiments were performed on sample surface polished and finished with 0.25 μm diamond paste. Polishing was undertaken after the irradiation process. Indentations were created across a range of forces, 1–50 N, with a minimum of five measurements taken at each value of force. Force was applied for a period of 20 s. The size of the resultant indentation was measured and used to calculate the hardness, H (in MPa), using Eq. (4). The lengths of the fractures radiating from the indentation were utilised to calculate the indentation fracture toughness, K_{Ic} using Eq. (5).

$$H = \frac{1.854mg}{d^2} \quad (4)$$

$$K_{Ic} = \frac{0.0824m}{c^{\frac{3}{2}}} \quad (5)$$

where m is the applied mass (in kg), d is the size of the indentation (in m), measured from the central point to the furthest point and c is the size of the fractures (in m), measured from the central point to their furthest extent. The indentation fracture toughness is not necessarily equal to fracture toughness measured by more conventional techniques, however, the indentation fracture toughness can be used successfully to rank the toughness of materials within a class or the effect of specific treatments on the toughness of a given material.

2.2. Spectroscopic techniques

Spectroscopic techniques were implemented to determine the effect of γ-irradiation upon glass structure and redox. Optical absorption spectroscopy was utilised to identify the colour generating absorption bands in the glasses. A Perkin Elmer Lambda 900 optical absorption spectrometer collected spectra over a range of 300–3300 nm. Experiments were performed on thin (30–100 μm thick), optically transparent glass slides which were polished to 1 μm. Differences in sample thickness were accounted for utilising the Beer–Lambert law.

FTIR (Fourier Transform Infra-Red) spectroscopy and Raman spectroscopy were used to quantify changes to the silicate network in response to γ-irradiation. A Perkin Elmer Spectrum 2000 FT-IR spectrometer was used with spectra being collected over 500–1500 nm. Experiments were performed by reflectance off the sample surface which had been polished to 1 μm. The subsequent results were then corrected through a Kronig–Kramers transform. A Renishaw InVia Raman microscope was used to collect spectra over a range of 0–1800 cm^{-1}. Results were acquired utilising laser (514 nm) excitation of samples polished to 1 μm.

Room temperature ^{57}Fe Mössbauer spectroscopy was applied to probe changes in Fe valence and coordination in response to γ-irradiation. A WissEl ^{57}Fe Mössbauer Spectrometer was used, operating in a constant acceleration mode and a ^{57}Co source (activity 9000 μCi, accounting for the decay of the source at time of experiment) was used as a radiation source. Samples were mixed with graphite to prevent excess absorption, and mounted in a perspex holder suitable for transmission, perpendicular to the incident radiation and the detector. Mössbauer spectra were fitted using two Lorentzian doublets, one each to represent the Fe^{2+} and Fe^{3+} environments, using the software package Recoil 1.03. The recoil free fraction was assumed to be equal in the Fe^{2+} and Fe^{3+} environments. Consequently, the area of the Lorentzian line shapes could be equated to the relative abundance of these oxidation states.

EPR spectroscopy was applied to characterise potential defect sites formed by γ-irradiation. An X-band Brüker EPR spectrometer with a field sweep of 0–800 mT at room temperature (~291 K) was used. Additional scans were performed over a field sweep of 330–350 mT at higher resolution in some samples. EPR experiments were performed on samples which were powdered to 75 μm. Samples were contained within a high purity silica tube during the experiment.

XAS (X-ray absorption spectroscopy) at the S K-edge and XES (X-ray emission spectroscopy) utilising S Kα emission were utilised to determine changes in sulphur valence and coordination within samples with significant sulphur content. These experiments were carried out at the ID26 beam line at the European Synchrotron Radiation Facility (ESRF), Grenoble. Samples were powdered to 75 μm and mounted onto an Al plate using acetone. The incident energy was controlled on the beamline utilising a fixed-exit double Si (1 1 1) crystal monochromator. Collimating and harmonic rejection mirrors were used to remove higher order harmonics. The theoretical resolution of the XAS experiment was 0.36 eV at the S K-edge. The energy was calibrated by using the absorption edge of natural S at 2472.0 eV. For XAS experiments the data were collected utilising a fluorescence detector mounted at 45° from the incident X-ray beam. The incident X-ray energy was varied over a range of 2450–2550 eV. XES experiments were carried out utilising a Johansson type crystal spectrometer employing a Si (1 1 1) crystal which was curved cylindricaly to meet a 500 mm Rowland circle radius, and a thermoelectrically cooled CCD detector (pixel size 22.5 × 22.5 μm^2) [29,30]. The incident photon energy was tuned to 2.52 keV. The sample surface was mounted at 45°, and the X-ray fluorescence was collected at 90° with respect to the incident beam direction. The energy calibration was performed relative to the Kα line of native S (2307.89 eV) which was used as a reference. The overall experimental energy resolution was ~0.4 eV, which was high enough to separate clearly between the S^{2-} and S^{6+} emission lines and quantitatively determine the proportion of reduced sulphur species in the sample. The latter was performed by fitting the measured XES spectra with a combination of two individual Lorentzian line shape doublets, corresponding to the emission lines associated with S^{2-} and S^{6+}, respectively [29,30].

3. Results

3.1. Mechanical techniques

3.1.1. Moduli

Figs. 1 and 2 show the Young's and shear moduli of the sample prisms as determined by the resonant frequency method described previously. The values of both moduli determined for the control

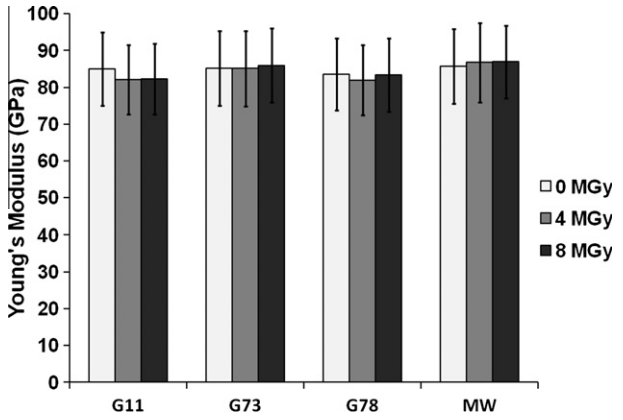

Fig. 1. Comparison of Young's modulus of control (0 MGy) and γ-irradiated (4 and 8 MGy) glasses determined by the resonant frequency technique. Error bars denote three standard deviations, as described in text.

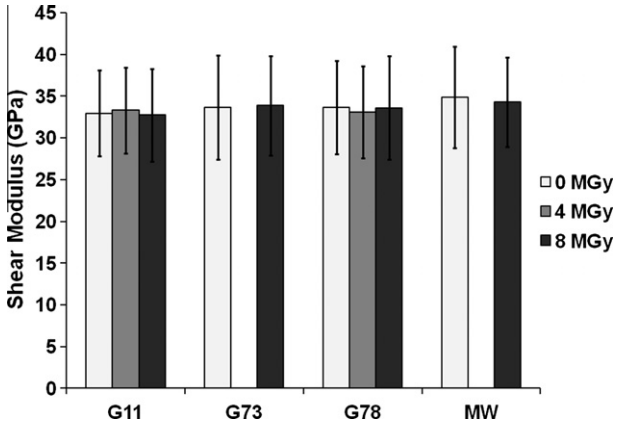

Fig. 2. Comparison of shear modulus of control (0 MGy) and γ-irradiated (4 and 8 MGy) glasses, determined by the resonant frequency technique. Data for G73 and MW-25% 4 MGy could not be obtained due to the dimensions of specimens for which a reliable standing wave could not be measured. Error bars denote three standard deviations, as described in text.

samples (0 MGy) are in good agreement with previous research [26], in which values of 78–81 GPa and 31–32 GPa respectively were reported for similar waste loaded compositions. The γ-irradiated specimens when compared with the un-irradiated control specimens show no significant change, within the precision of the measurements. In contrast, previous γ-irradiation studies of alkali-borosilicate glasses reported a significant increase in density and hence Young's and shear modulus, due to increased network polymerisation [27], as discussed further in Section 4.1. The error bars shown in Figs. 1 and 2 represent the propagated errors associated with measurement of the dimensions, density and resonant frequency of the glass prisms, based on at least three independent measurements.

Fig. 3 shows Poisson's ratio, ν, determined from the Young's and shear moduli utilising Eq. (3). Given the agreement between the values of Young's and shear moduli for the current and previous work it is not surprising that the values of Poisson's ratio determined for the control glass samples are in good agreement with values previously reported for glasses of similar compositions (for which $\nu \approx 0.25$) [26]. In addition, it is not surprising that there is no significant change in the value of Poisson's ratio as a consequence of γ-irradiation, given that shear and Young's moduli are unchanged within precision. The error bars quoted in Fig. 3 represent the propagated errors associated with measurement of the Young's modulus and the shear modulus of the glass prisms.

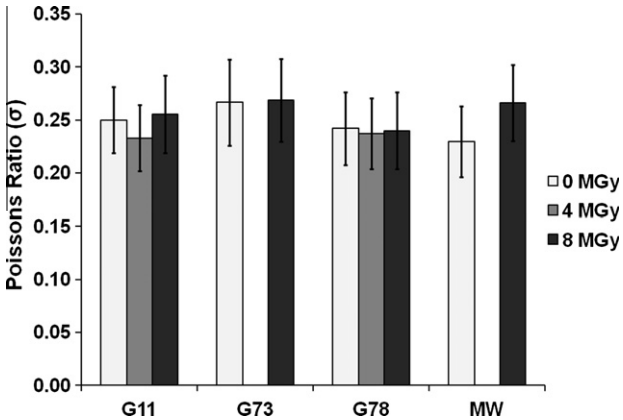

Fig. 3. Comparison of Poisson's ratio for the control (0 MGy) and γ-irradiated (4 and 8 MGy) glasses. Derived from the Young's and shear modulus using Eq. (3). Data for G73 and MW-25% 4 MGy results are not shown due to absence of satisfactory shear modulus data. Error bars denote three standard deviations, as described in text.

3.1.2. Hardness

Fig. 4 shows the hardness values as determined from micro-indentation of the glass surfaces. The hardness values for the control samples were in good agreement with results from previous research which reported values of 5.9–7.1 MPa for similar compositions [28]. The hardness values determined for the γ-irradiated glass samples showed no significant variation from the values obtained for the control samples (0 MGy) within the estimated precision of the measurements. These results are consistent with past observations of alkali-borosilicate glasses, albeit at lower doses (1 MGy) [9,27]. The error bars reported in Fig. 4 were derived from the standard deviation of the 30–50 results obtained for each sample.

3.1.3. Indentation fracture toughness

Fig. 5 shows the indentation fracture toughness of the samples as determined through micro-indentation of the glass surface. The samples were not annealed prior to the measurement of fracture toughness which would otherwise heal any defects induced by γ-irradiation. Therefore, although the absolute values of indentation fracture toughness may be subject to systematic error, relative changes in indentation fracture toughness are considered meaningful. The indentation fracture toughness values obtained for the

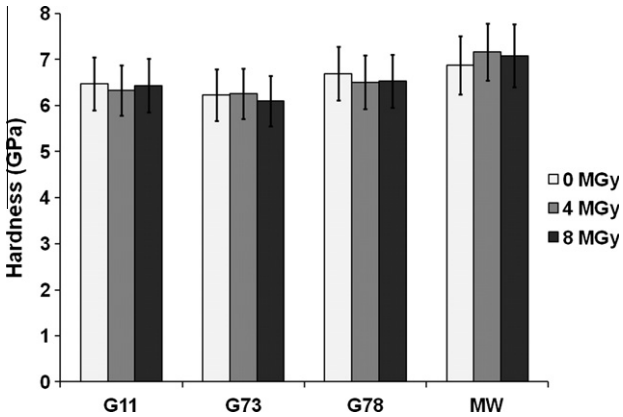

Fig. 4. Comparison of hardness values in control (0 MGy) and γ-irradiated (4 and 8 MGy) glasses. Determined through Vicker's indentation experiments across a range of indentation forces from 1 N to 50 N. Error bars denote three standard deviations, as described in text based on at least 30 measurements, as described in text.

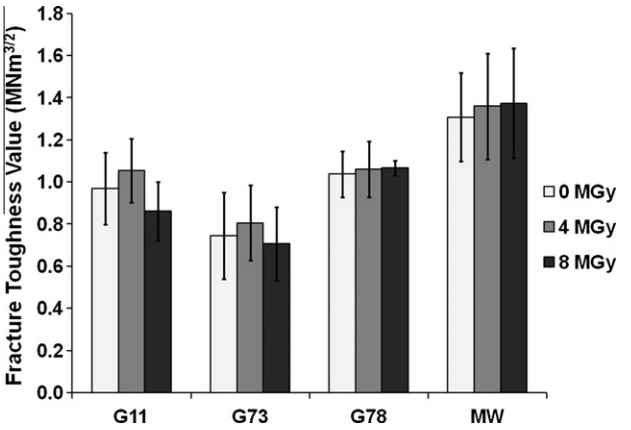

Fig. 5. Comparison of indentation fracture toughness values in control (0 MGy) and γ-irradiated (4 and 8 MGy) glasses. Determined through Vicker's indentation experiments across a range of indentation forces. Error bars denote three standard deviations, as described in text based on at least 30 measurements, as described in text.

control glass samples (0 MGy) are in good agreement with previous research [28] in which values of 0.81–1.06 $Nm^{-3/2}$ were reported. Within the estimated precision of the measurements, the γ-irradiated glass samples presented no significant variation in fracture toughness when compared with the results determined from the control samples. These results are broadly consistent with previous studies of alkali-borosilicate glasses, albeit at lower doses (1 MGy) [9,27]. The errors bars reported in Fig. 5 were derived from the standard deviation of the 30–50 results obtained for each sample.

3.2. Spectroscopic techniques

3.2.1. Optical absorption spectroscopy

A clear non-linear variation in colour was observed in the samples MW-25% and G73, in response to increased radiation dose. In glass G73 the shade increased in darkness in the order 8 MGy < 0 MGy < 4 MGy, and in the order 0 MGy < 4 MGy ≈ 8 MGy in the MW-25% glass sample. The variation in glass G73 is displayed in Fig. 6.

Optical absorption spectroscopy was applied to identify γ-radiation induced changes in absorbing species.

3.2.1.1. Optical absorption in glass G11 and G78. Figs. 7 and 8 show the optical absorption spectra for glasses G11 and G78. Two absorption bands are apparent in the spectra of both glasses; a broad band centred at *ca.* 1000 nm and a comparatively narrow absorption band at *ca.* 450 nm. Both of these bands can be attributed to absorption from Fe species within the glass, the former

Fig. 6. Photographic image of 75 μm powder samples of glass G73 (0, 4 and 8 MGy). Variation in colour induced by γ-irradiation is clearly observed. (For interpretation of the references to colour in this figure legend, the reader is referred to the web version of this article.)

to Fe^{2+} species, specifically those in distorted octahedral coordination environments, and the latter to Fe^{3+} species [31]. The UV edge in these glasses, visible at the lower extreme of wavelengths, is prominent at a higher wavelength than is typical in alkali-borosilicate glasses. This can be attributed to the high Fe content of these glasses, which is known to bring the UV edge to longer wavelengths [31]. The bands identified are in good agreement with those reported to be present in similar high Fe content alkali-borosilicate glasses, where bands related to Fe^{2+} have been identified at 1075 nm and at 2000 nm, and Fe^{3+} bands have been identified at 380 nm, 415 nm, 435 nm, and 445 nm [31–33]. Overall, inspection of Figs. 7 and 8 demonstrates that the optical absorption spectra do not show any significant change as a consequence of γ-irradiation.

3.2.1.2. Optical absorption in glass G73. Fig. 9 displays the optical absorption spectra for the glass G73. Three absorption bands are apparent in the spectra of the control sample (0 MGy); one broad band centred at approximately 1000 nm, which can be attributed to Fe^{2+} in a distorted octahedral coordination, another at 450 nm which can be attributed to Fe^{3+} species [33], and a third at approximately 650 nm. This third band is attributable inter-valence charge transfer between Fe^{3+} and Fe^{2+} across a bridging oxygen (Fe^{2+}–O–Fe^{3+}) [31]. This band has been observed in Fe rich alkali-borosilicate glasses in previous studies [31].

The γ-irradiated G73 samples present only two significant absorption bands, those at 1000 nm and 450 nm which have been attributed to Fe^{2+} and Fe^{3+} respectively [33]. The inter-valence transfer band is absent from these samples. In this respect, the optical absorption spectra of the γ-irradiated G73 samples are in good agreement with the G11 and G78 samples as well as the majority of comparable reduced high Fe alkali-borosilicate glasses, such as those reported in [31–33]. Notably, the UV edge is also apparent at longer wavelengths in the un-irradiated G73 glass samples.

3.2.1.3. Optical absorption in glass MW-25%. Fig. 10 shows the optical absorption spectra of the glass MW-25%. One strong absorption band is present at approximately 450 nm, and three weaker absorption bands at 580 nm, 745 nm and 805 nm. As in the glasses G11, G73 and G78, the band at 450 nm can be attributed to Fe^{3+}. The three weaker bands are consistent with absorption by Nd^{3+} ions [34]. Notably, the absorption band related to Fe^{2+} at 1000 nm was absent. These results show, in general, good agreement with published literature relating to high Fe content alkali-borosilicate glasses as has been reported in [31–33]. The notable features of this glass, namely the absence of the Fe^{2+} optical absorption band and the presence of Nd^{3+} optical absorption bands, can be attributed to the HLW simulant waste loading, which lacks the high organic content of the ILW simulant waste, that acts as a carbonaceous reductant, but instead contains rare earth elements, such as Nd. Overall, inspection of Fig. 10 demonstrates that the optical absorption spectra do not present any significant change as a consequence of γ-irradiation.

3.2.2. FTIR spectroscopy

FTIR spectroscopy was applied to probe potential changes in glass structure induced by γ-irradiation. FTIR spectra were fitted using Gaussian line-shapes assigned to well established IR absorption bands, as summarised in Table 2. Fig. 11a–d shows the FTIR spectra of the samples and the associated fits based on previous literature assignments. The primary absorption bands were associated with Si–O–Si bending and stretching modes (~455 cm^{-1} and ~1000 cm^{-1}), B–O–B bending and stretching modes associated with BO_3 units (~720 cm^{-1} and ~1370 cm^{-1}) and Fe–O bending modes (~550 cm^{-1}). These assignments are in good agreement with previous investigations of alkali-borosilicate glasses

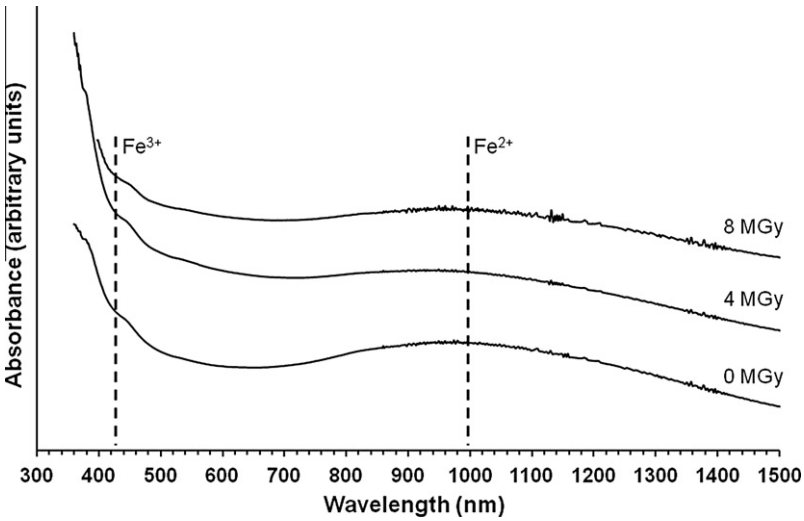

Fig. 7. Comparison of optical absorption spectra in control (0 MGy) and γ-irradiated (4 and 8 MGy) samples from glass G11. Data are the sum of three averaged optical absorption spectra taken from different areas of a transparent section; for clarity data are offset on the *y*-axis.

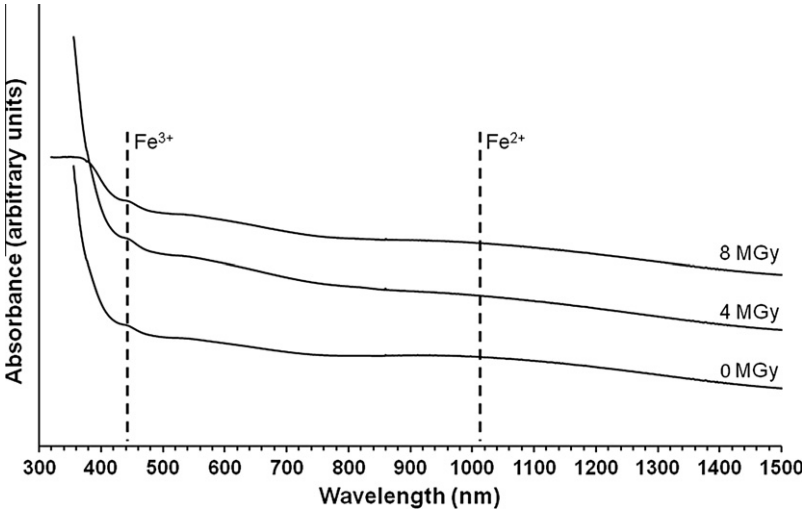

Fig. 8. Comparison of optical absorption spectra in control (0 MGy) and γ-irradiated (4 and 8 MGy) samples from glass G78. Data are the sum of three optical absorption spectra taken from different areas of a transparent section; for clarity data are offset on the *y*-axis.

[35,36,38–42], and specifically Fe-rich alkali-borosilicates [39]. Additional bands were present in the G78 and MW-25% glass samples at 800 cm^{-1} and 1275 cm^{-1} respectively; these were fitted to B–O–B bending and stretching modes in BO_4 units [36–38]. The intensity of this band was observed to be strongly correlated to higher boron content and the presence of BO_4 units.

The position of the broad Si–O–Si stretching mode of the G11, G78 and MW-25% was always within 7 cm^{-1} of 992 cm^{-1}, in reasonable agreement with the typical range of 950–970 cm^{-1} expected for high Fe alkali-borosilicate glasses [38,39]. The appearance of this band is characteristic of a distribution of unresolved Q^n species. In contrast, glass G73 presented two well resolved Si–O–Si stretching modes centred at 921 cm^{-1} and 1017 cm^{-1}. This implies that the Q speciation of glass G73 is strongly affected by the alkaline-earth content of the glass, which produces a high proportion of Q^2 units that can be distinguished from the distribution otherwise dominated by the (alkali-associated) Q^3 units typically present in alkali-borosilicate glasses. This conclusion is consistent with available data for related Ba-rich borosilicate glasses [43], in which clearly resolved Si–O–Si stretching modes attributed to Q^2 and Q^3 species were apparent.

Across all four glasses, no significant variation in the distribution of IR bands was apparent between the control (0 MGy) and the γ-irradiated samples. As discussed in Section 4.2, previous FTIR studies of γ-irradiated alkali borosilicate glasses pointed to a marked change in Q speciation and hence network polymerisation [27]. In the present study, however, the lack of detectable change in Q speciation, as a consequence of γ-irradiation, is wholly consistent with the observed invariance in mechanical properties presented in Section 3.

3.2.3. Raman spectroscopy

Raman spectroscopy was also applied to probe potential changes in glass structure induced by γ-irradiation. Raman spectra were fitted using Gaussian line-shapes assigned to well established Raman modes, as summarised in Table 3. Fig. 12a–d shows the Raman spectra of the samples and the associated fits. The most significant Raman bands were related to Si–O–Si stretching modes assigned to specific Q units (~871–1140 cm^{-1}), Si–O–Si bending modes (490 cm^{-1}), B–O–B stretching modes (~1390 cm^{-1}), to borosilicate ring breathing modes (~570 cm^{-1} and ~650 cm^{-1}), and Fe^{3+}–O stretching modes (~920–945 cm^{-1}) [45,53,54]. These

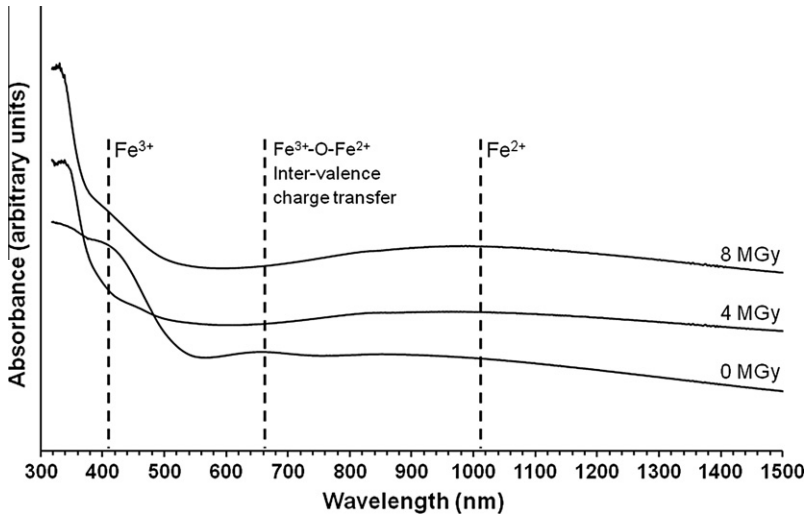

Fig. 9. Comparison of optical absorption spectra in control (0 MGy) and γ-irradiated (4 and 8 MGy) samples from glass G73. Data are the sum of three optical absorption spectra taken from different areas of a transparent section; for clarity data are offset on the *y*-axis.

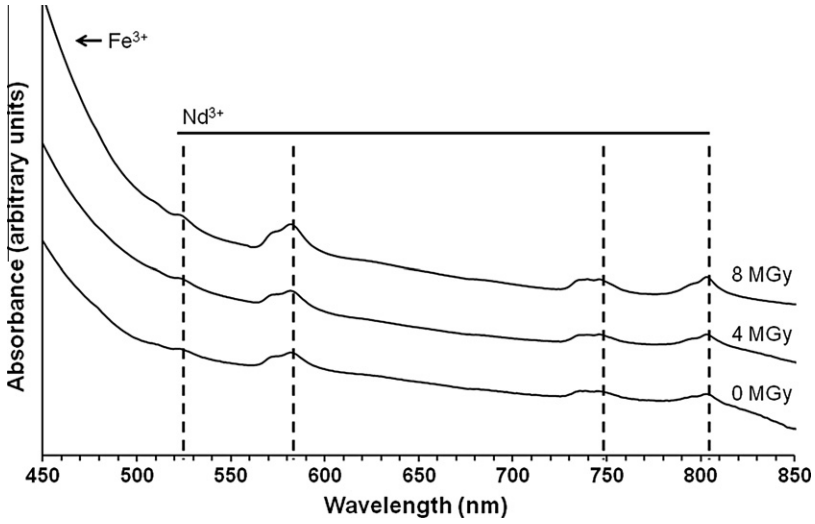

Fig. 10. Comparison of optical absorption spectra in control (0 MGy) and γ-irradiated (4 and 8 MGy) samples from glass MW-25%. Data are the sum of three optical absorption spectra taken from different areas of a transparent section; for clarity data are offset on the *y*-axis.

Table 2
Assignment of FTIR bands.

Band position (cm^{-1})	Band assignment	References
450–480	Si–O–Si bending	[35–39]
555–560	Fe^{3+}–O stretch	[38,39]
705–730	B–O–B (BO_3) bending	[38–40]
798–800	B–O–B (BO_4) bending	[38–40]
860–870	Si–O–NB Q_0 stretching	[46]
920	Si–O–NB Q_1 stretching	[35,41]
985–1020	Si–O–Si stretching	[35,39–42]
1135–1160	Si–O–NB Q_3 stretching	[33,38]
1275	B–O–B (BO_4) stretching	[33–40]
1365–1385	B–O–B (BO_3) stretching	[38–40]

band assignments are in good agreement with Raman observations of alkali-borosilicate glasses, and Fe-rich alkali borosilicate glasses [45,46,48–55]. In addition to the aforementioned bands, a strong band located at 990 cm^{-1} was detected in glasses G11 and G73, and fitting of data from glass G78 also indicated a contribution from a band at ~990 cm^{-1}; however, this band was absent from the glass MW-25%. The 990 cm^{-1} band is attributed to the S–O stretching mode in the SO_4^{2-} oxyanion, typically when associated with alkali species such as Na, based on previous reports [44–47,56]. An additional Raman band was apparent at ~400 cm^{-1} in the spectra of glasses G11, G73, and G78, which was attributed to the Fe^{3+}–S^{2-} stretch, based on the analysis of Klimm [58] and several mineralogical examples of metal sulphides [59–61]. Fig. 13 shows the variation in intensity of the fitted 400 cm^{-1} band. The absence of the 990 and 400 cm^{-1} bands in the Raman spectra of MW-25% glass, is consistent with the negligible sulphur content of this composition.

Comparison between the control glass samples (0 MGy) and the γ-irradiated samples showed no significant variation between the bands associated with Si or B derived modes, associated with the glass network, consistent with the results of FTIR analysis. Comparison of the G11, G73 and G78 control samples and the γ-irradiated samples show significant band variations at 400 cm^{-1}. This is clearly reduced in intensity post γ-irradiation, most significantly in glass G73. This reduction points to a decrease in the volume fraction of the Fe^{3+}–S^{2-} species as a consequence of γ-irradiation.

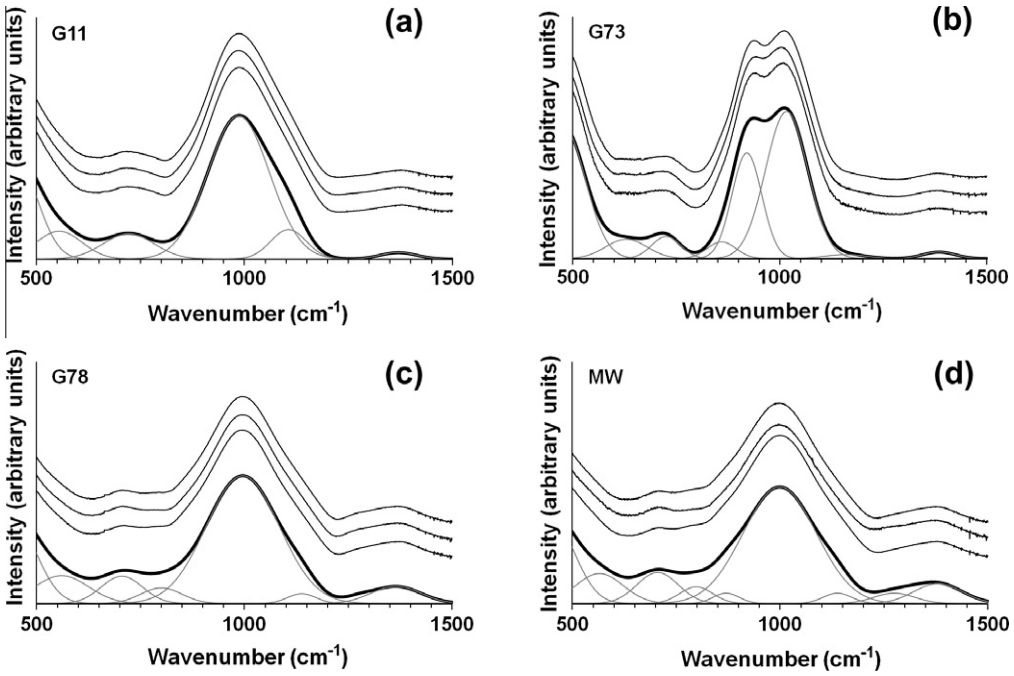

Fig. 11. (a–d) Comparison of FTIR spectra in control (0 MGy) and γ-irradiated (4 and 8 MGy) samples. Data are the sum of three FTIR spectra from each sample; for clarity data are offset on the *y*-axis in order of increasing dose (from 0 to 8 MGy). The bold line corresponds to the sum of fitted the Gaussian contributions in grey.

Table 3
Assignment of Raman bands.

Band position (cm^{-1})	Band assignment	References
400–420	Sulphide (Fe^{3+}–S^{2-})	[44–47]
480–500	Si–O–Si bending mode	[46,47,49–53]
570–650	Borosilicate ring breathing mode	[46,47,49]
860–880	Si–O–Si stretching Q_1	[45,49–55]
910–930	Si–O–Si stretching Q_2	[45,49,50,52–54,56,57]
940–950	Fe^{3+}–O stretching	[47,55–56]
990	S–O stretching (S^{6+})	[43–45,55]
1020–1040	Si–O–Si stretching Q_3	[46,47,49–55,57]
1090–1110	Si–O–Si stretching Q_3·	[45–47,49,50,54–55]
1160–1180	Si–O–Si stretching Q_4	[45,47,49,51–55,57]
1380–1400	B–O–B stretching	[47,49,51]

3.2.4. ^{57}Fe Mössbauer spectroscopy

^{57}Fe Mössbauer spectroscopy was used to quantify potential variation in Fe oxidation state induced by γ-irradiation. In addition, examination of the dipole and quadrupole splitting associated with the fitted Mössbauer spectra was used to determine the possible change in average Fe coordination induced by γ-irradiation.

3.2.4.1. Quantification of Fe oxidation state. Fig. 14a–d shows the Mössbauer spectra for the glasses G11, G73 and G78. The spectra show two convoluted doublet signals, indicating the presence of Fe in mixed valence state in these glasses. Fig. 14d shows the Mössbauer spectra for the MW-25% glasses, a single doublet was apparent, showing only Fe^{3+} is present in these materials. Fig. 15 shows the relative quantity of Fe^{2+} relative to the overall Fe content of the glasses, as derived from the areas of the fitted Lorentzian lineshapes, which can be assigned to Fe^{2+} or Fe^{3+} species. Comparison of the three glasses shows that glass G73 has a volume fraction of Fe^{2+} that is 25% greater than G11 or G78. These results are in line with prior expectation, as glasses loaded with highly reducing organic waste (G11, G73 and G78) contain partially reduced Fe, whereas Fe in the MW-25% glass is fully oxidised due to the absence of organic reducing agents in the simulant HLW. The higher extent of Fe reduction in G73 can be linked to the lower content of Fe in this glass, compared to G11 or G78, relative to the waste loading which was equivalent across all three glasses.

Fig. 15 also shows a comparison of the extent of Fe reduction in the control samples (0 MGy) against the γ-irradiated samples. There was no significant change in the Fe oxidation state between the control and the γ-irradiated samples, within the estimated limits of error, consistent with a previous Mössbauer study of the effect of γ-irradiation on Fe redox in borosilicate glasses [21]. The errors described were determined from the standard deviation of the peak areas of three independent measurements.

3.2.4.2. Changes in Fe coordination environment. Fig. 16 shows the average dipole (δ) and quadrupole (Δ) splitting of the Fe^{2+} and Fe^{3+} species present in the samples, based upon the Lorentzian fitting of the spectra. The splitting values for the Fe^{2+} environment in all samples shows there is no significant change within the estimated error across the range of γ-radiation doses. The splitting values for Fe^{3+} sites in the glasses G11 and G78 also show no measurable change within the estimated errors across the range of γ-irradiation doses. Fe^{3+} environments within the MW-25% glass present a statistically significant decrease in quadrupole splitting (0.10 ± 0.02 mm s^{-1}) with γ-irradiation between 0 MGy and 4 MGy, no subsequent variation is apparent, within the limits of precision. Fe^{3+} environments in glass G73 present no significant variation in coordination between 0 MGy and 4 MGy, within the estimated errors, however a significant decrease in quadrupole splitting is apparent between 4 MGy and 8 MGy (0.11 ± 0.02 mm s^{-1}). The results in G73 and MW-25% results are consistent with investigation of Eissa et al. [21], which reported comparable changes in Fe^{3+} quadruple splitting in Fe rich Na-borosilicate glasses as a consequence of γ-irradiation.

3.2.5. EPR spectroscopy

EPR spectroscopy was used to probe defects produced by the process of γ-irradiation within the glasses. In addition, EPR

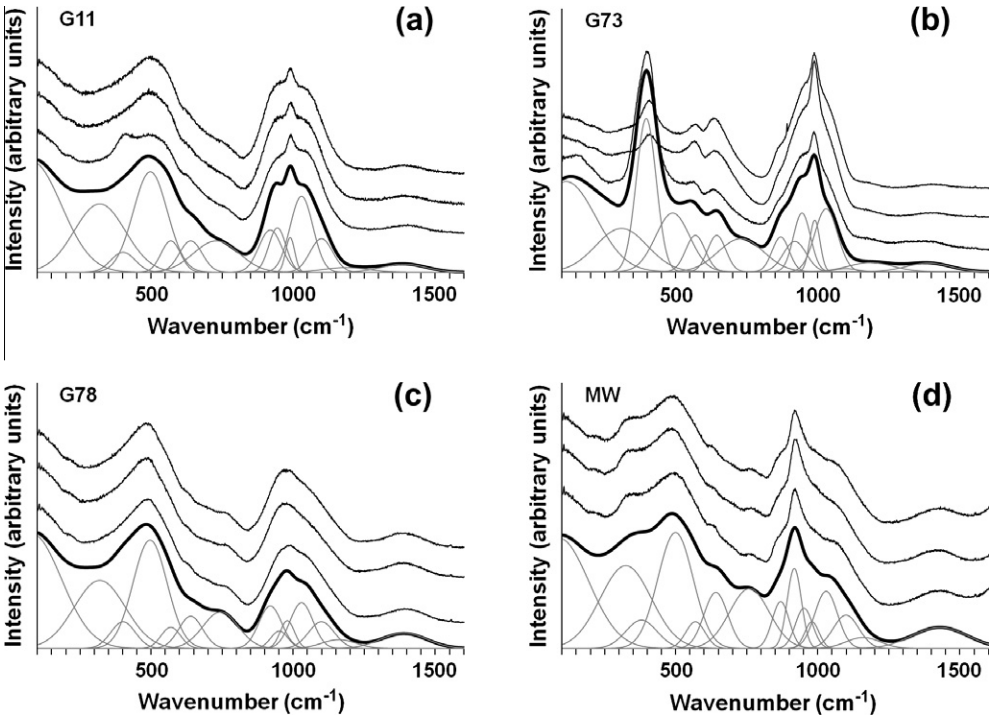

Fig. 12. (a–d) Comparison of Raman spectra in control (0 MGy) and γ-irradiated (4 and 8 MGy) samples. The radiation dose increases towards the top of the graph. Data are the sum of three Raman spectra from each sample; for clarity data are offset on the *y*-axis in order of increasing dose (from 0 to 8 MGy). The bold line corresponds to the sum of the fitted Gaussian contributions in grey.

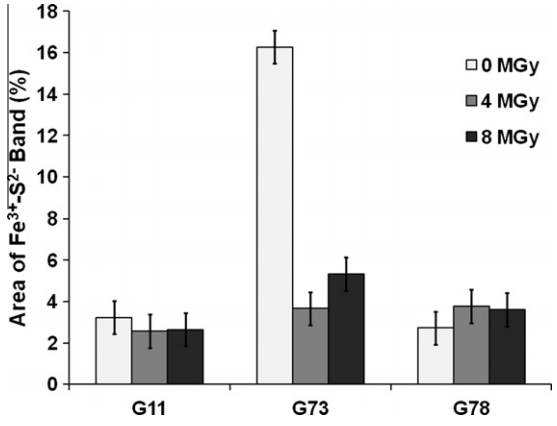

Fig. 13. Variation in 400 cm^{-1} band area relative to total fitted area of spectra, between control (0 MGy) samples and γ-irradiated (4 and 8) MGy samples, in glasses G11, G73 and G78. Error bars based on estimated precision of fit.

spectroscopy allowed the Fe^{3+} environment to be studied, and other paramagnetic species to be detected.

Fig. 17 shows the EPR spectra for the glasses G11, G73 and G78 un-irradiated (0 MGy) and γ-irradiated (4 and 8 MGy). Previous studies of γ-irradiated alkali-borosilicate glasses [62] reported the presence of boron oxygen hole centres (BOHCs) identified by a strong and sharp EPR signal near $g_{eff} \approx 2.0$. These signals were absent from the EPR spectra of the γ-irradiated glasses reported here, in both the broad scans shown in Fig. 17 and in high resolution scans of the $g_{eff} \approx 2.0$ region. Olivier et al. reported that EPR signals associated with BOHCs, generated by ionising β-radiation, decrease in intensity in proportion to increasing Fe content [63]. Thus, the absence of sharp signals at $g_{eff} \approx 2.0$ in the plots displayed in Fig. 17 may be a consequence of the Fe mediated healing of such defects, as discussed in Section 4.3.

Two intense but broad EPR signals were detected from all samples at $g_{eff} \approx 2.0$ and $g_{eff} \approx 4.3$. The signal at $g_{eff} \approx 2.0$ was unrelated to the signature signal of BOHCs. These signals have been attributed to the Fe^{3+} species; specifically to Fe^{3+} in clustered regions in which Fe^{3+} ions are in close enough proximity for exchange interactions to dominate, or to regions in which Fe^{3+} is in isolated distorted tetrahedral or octahedral sites for $g_{eff} \approx 2.0$ and $g_{eff} \approx 4.3$ respectively [31]. A further signal was evident in the glasses at approximately $g_{eff} \approx 6.3$ which has also been attributed to Fe^{3+} environments, ostensibly in which one or more coordinating anion is not O^{2-}. Therefore, this signal may be associated with the Fe^{3+}–S^{2-} species, although a definite connection has not been proven [31]. The presence of these signals is in general agreement with established knowledge for Fe containing borosilicate glasses [62–64].

Table 4 shows the intensity ratio of the $g_{eff} \approx 2.0$ Fe^{3+} signal against the Fe^{3+} $g_{eff} \approx 4.3$, for each EPR spectrum, based upon the assumption that there is no significant change in the width of the observed EPR peaks. By analysing the peak to peak intensity (I_{p-p}) of the Fe^{3+} signal the variation in Fe^{3+} environment and distribution of Fe^{3+} environments can be ascertained for each sample. The reported variations in I_{p-p} between the three glasses are in good agreement with work conducted by Bingham et al. [66] and can be attributed to the quantity and ionic radius of alkali and alkaline-earth species which are present in glass compositions. The presence of alkali ions in the glass can be linked to the increase in the prevalence of Fe^{3+} in clustered sites, increasing the signal at $g_{eff} \approx 2.0$. This correlates with the known compositions of the G11 and G78 samples, where increased Na content in G11 leads to an increase in the $g_{eff} \approx 2.0$ signal relative to that at $g_{eff} \approx 4.3$. The G73 results show a weak $g_{eff} \approx 2.0$ signal relative to $g_{eff} \approx 4.3$, this is attributable to the high Ba content of this glass, since large alkali-earth ions have been identified as being less effective at causing Fe^{3+} cluster formation [31]. In comparing the I_{p-p} results, presented in Table 4, for the control glass (0 MGy) and the γ-irradiated glasses (4 and 8 MGy), it can be seen that there is no significant variation in I_{p-p} in response to γ-radiation.

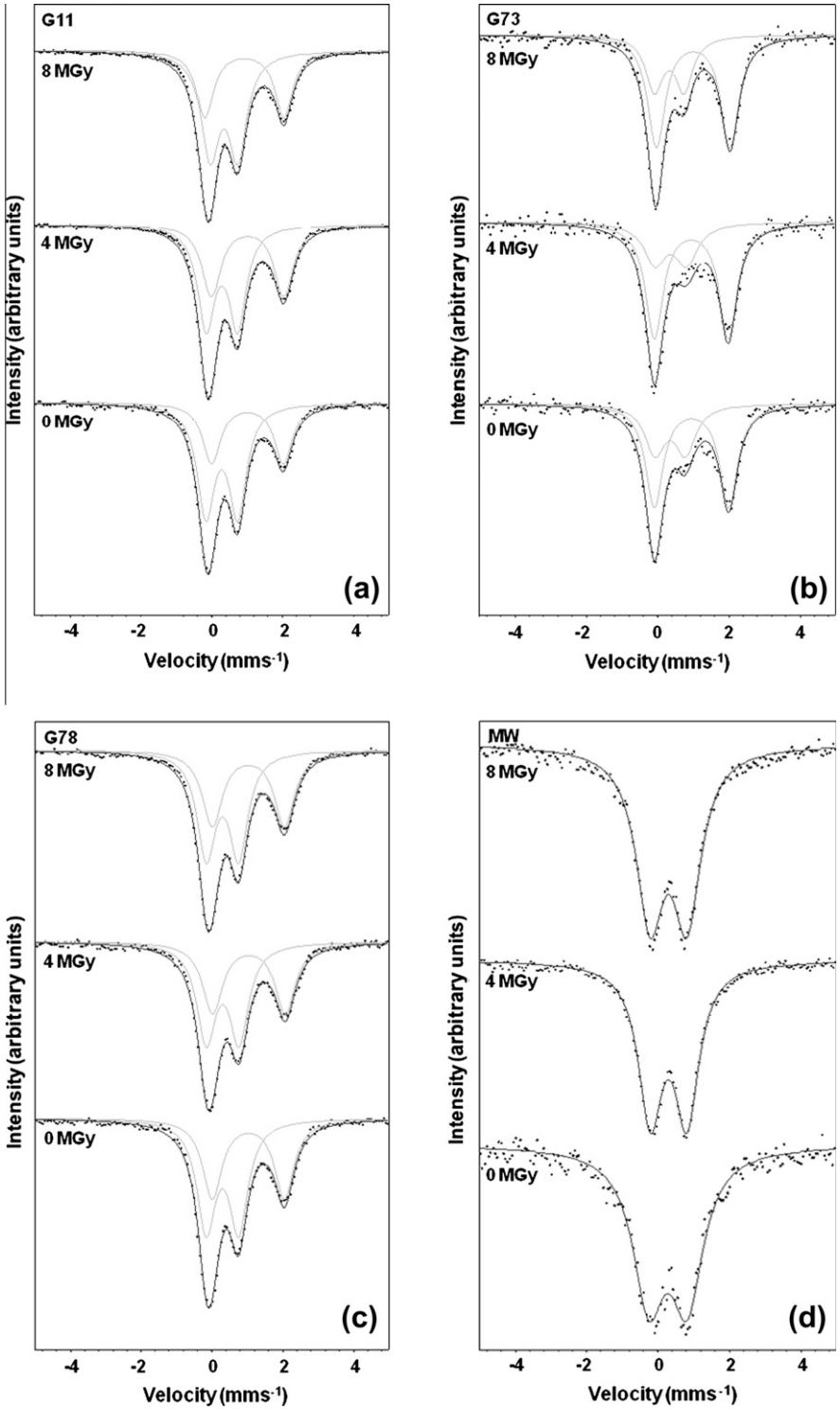

Fig. 14. (a–d) Comparison of ^{57}Fe Mössbauer data (solid points) in control (0 MGy) and γ-irradiated (4 and 8 MGy) samples fitted with Lorentzian doublets (lines); note, only a single doublet fitted to spectrum 14d.

A unique signal was noted in the 4 MGy sample of G78 at $g_{eff} \approx 2.8$. Possible explanations for this signal are that it is related to ferro-magnetic inclusions present in the glass [67], the presence of anti-ferromagnetic coupling between Fe^{3+} and Fe^{2+} [65], both of which are present in these glasses, or the presence of a high symmetry Fe^{3+} resonant centre [68].

3.2.6. X-ray absorption spectroscopy and X-ray emission spectroscopy

X-ray absorption spectroscopy and X-ray emission spectroscopy at the sulphur K-edge were applied in order to determine the oxidation state and environment of sulphur within the glasses G11, G73 and G78. The MW-25% set was excluded as it contained a negligible quantity of sulphur.

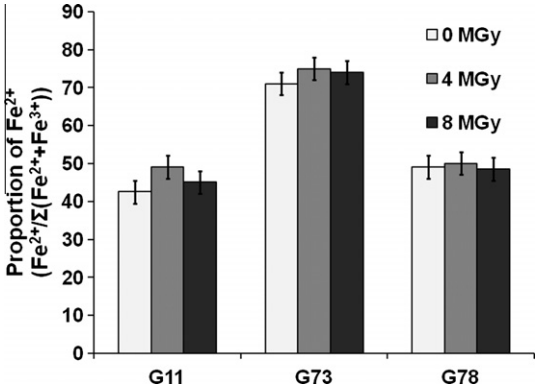

Fig. 15. Comparison of Fe oxidation state in control (0 MGy) and γ-irradiated (4 and 8 MGy) glasses derived from Lorentzian fitting of Mössbauer spectra. Error bars represent an error of ±2% derived from the associated data fitting method.

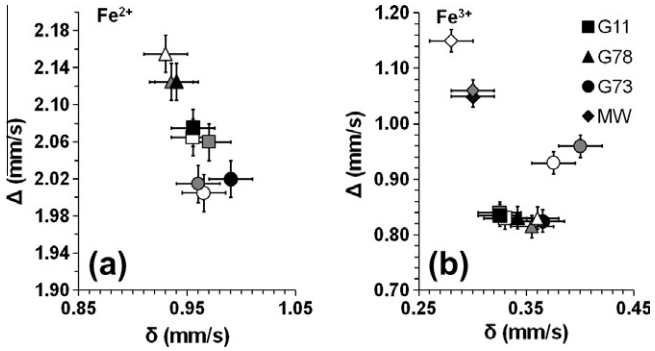

Fig. 16. (a and b) Comparison of Fe dipole (δ) and quadrupole (Δ) splitting in control (0 MGy) and γ-irradiated (4 and 8 MGy) glasses; open, grey and black symbols correspond to dose of 0, 4, and 8 MGy, respectively. Errors bars represent three standard deviations, derived from the fitting of three individual spectra.

3.2.6.1. X-ray absorption spectroscopy. Fig. 18 shows the X-ray absorption spectra for the three glasses over the XANES (X-ray Absorption Near Edge Structure) region. The spectra are the result of a convolution of two or more absorption spectra relating to sulphur in different oxidation states. The strong feature present in all spectra at 2482 eV is related to sulphur in the S^{6+} oxidation state in good agreement with both sulphate standards and with the work of Bingham et al. [66]. The features present from 2468 to 2472 eV are associated with sulphur in a more reduced environment matching closely to spectra of sulphide (S^{2-}) standards reported by Bingham et al. [66]. It is probable the intermediate oxidation states of sulphur are present in these spectra, such as sulphite (S^{4+}) which can be attributed to the weak feature present at ~2478 eV [66]. The pre-edge and edge region of the X-ray absorption spectra were fitted to a range of sulphur standards in an effort to identify a chemical analogue for the interaction of the reduced sulphur with the glass. However, fitting was inadequate for the quantification of the sulphur oxidation state due to strong post-edge features seen with the sulphur standards, which were absent in the glass spectra.

The features associated with reduced sulphate species in glass G73 are notably different to those observed in G11 and G78. The features associated with reduced sulphur species in G11 and G78 approximately match those of As_2S_3, implying the presence of sulphide (S^{2-}) [66]. The features associated with reduced sulphur species in glass G73 approximately match the spectra of the $CuFeS_2$ and Cu_5FeS_4 [66]. The features observed in the case of the G73 glass show good agreement with observations made by Backnaes et al. [69] which proposed sulphur coordination to transition metals.

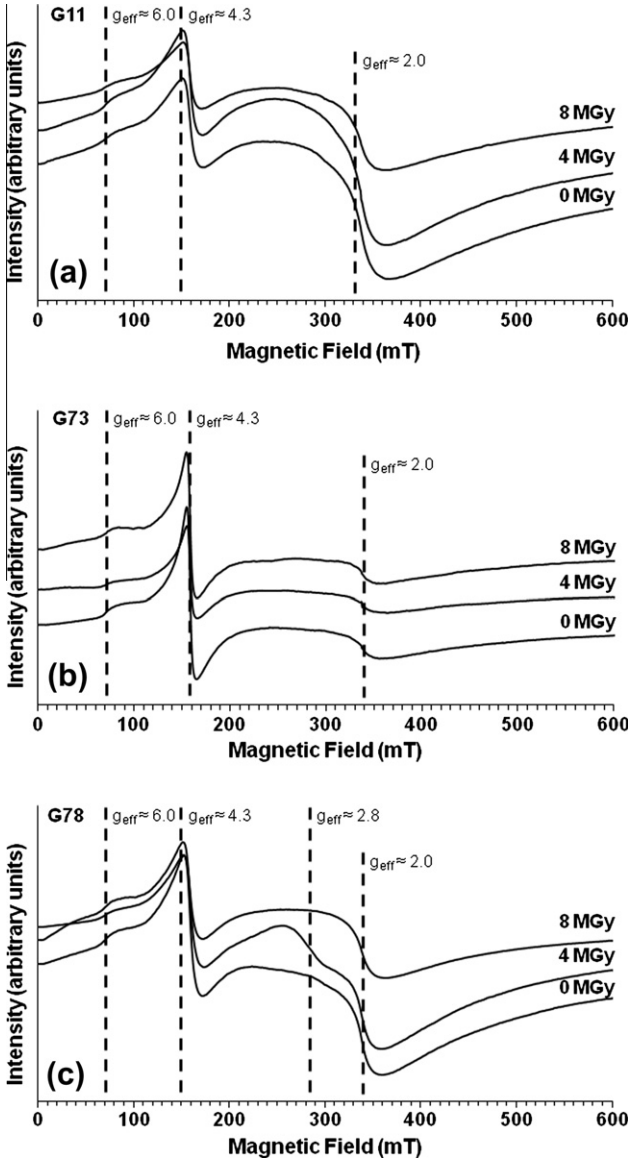

Fig. 17. (a–c) Comparison of EPR spectra in control (0 MGy) and γ-irradiated (4 and 8 MGy) samples from glass G11, G73 and G78; for clarity data are offset on the *y*-axis.

Table 4
Peak to peak intensity ratio variation across radiation doses derived from EPR spectra. Errors derived from systematic errors based on estimation of peak intensity.

Glass	Intensity ratio I_{p-p} ($g_{eff} \approx 2.0/g_{eff} \approx 4.3$)		
	0 MGy	4 MGy	8 MGy
G11	1.54 ± 0.10	1.40 ± 0.10	1.24 ± 0.10
G73	0.18 ± 0.10	0.23 ± 0.10	0.15 ± 0.10
G78	0.77 ± 0.10	0.99 ± 0.10	0.82 ± 0.10

This suggests that the reduced sulphur species present in the G73 glass may be coordinated to the glass network *via* a transition metal atom, most probably Fe, and that they are in the sulphide oxidation state (S^{2-}). This is consistent with Raman spectroscopy results discussed in Section 5.2.

3.2.6.2. X-ray emission spectroscopy. Fig. 19a–c shows the XES data collected for the control (0 MGy) samples compared with those from the γ-irradiated (4 and 8 MGy) samples. The proportion of re-

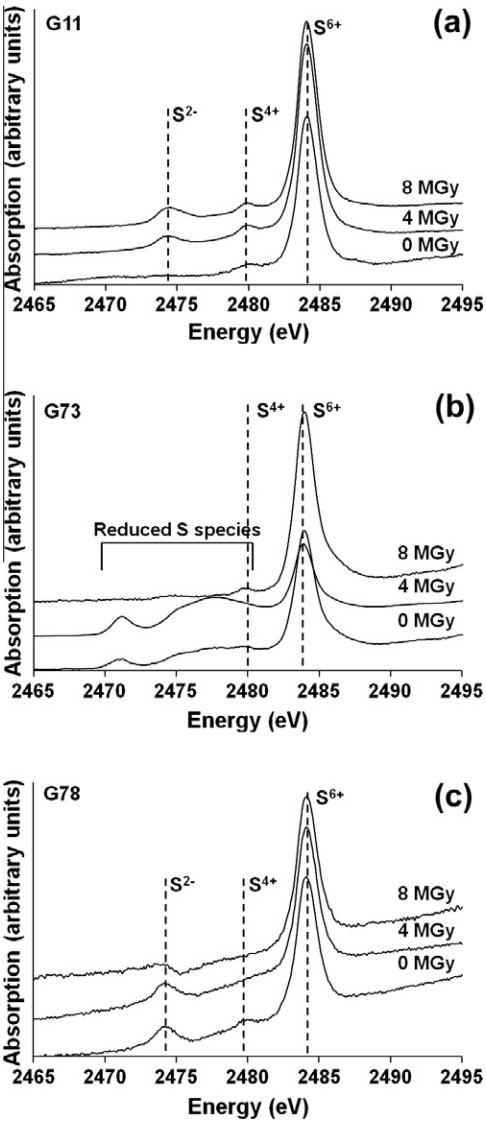

Fig. 18. (a–c) Comparison of SK-edge XANES spectra in control (0 MGy) and γ-irradiated (4 and 8 MGy) samples from glass G11, G73 and G78; for clarity data are offset on the *y*-axis.

duced sulphur species can be seen to vary in all three glasses in response to γ-irradiation. This variation cannot be quantified by fitting of the XANES region which is more sensitive to the local coordination environment, in contrast to XES. The X-ray emission spectra in Fig. 19 were fitted with Lorentzian line shape and the intensity ratio of the $K\alpha_{1,2}$ doublets was constrained to be constant [29,30].

Fig. 20 shows the proportion of S^{2-} relative to the overall proportion of sulphur in the glasses G11, G73 and G78 across all γ-irradiation doses. In the glass G11 no variation is apparent within the estimated limits of error, whereas, in glass G73 and G78 a clear variation in the sulphur oxidation state is apparent, which is consistent with the qualitative XAS observations. Glass G78 shows a linear increase in the proportion of S^{2-} with respect to the applied radiation dose, whereas glass G73 shows a non-linear trend with an increase in S^{2-} from 45% to 71% at 4 MGy, and a decrease to 13% at 8 MGy (estimated precision of ± 5%). This trend parallels the observed variation in colour observed in the powdered samples, increasing in the order 8MGy < 0 MGy < 4MGy. Variations in sulphur oxidation state induced by γ-irradiation have not been previously reported to the best of our knowledge.

4. Discussion

4.1. Mechanical property variation

Comparison of the mechanical properties of the control glass samples (0 MGy) against the γ-irradiated samples, Section 3, showed that there was no significant change in Young's modulus, shear modulus, hardness or fracture toughness. This behaviour is not typically observed in simplified alkali-borosilicate compositions, where γ-irradiation typically results in increased density with concomitant change in the mechanical properties [27]. According to Shelby et al. [27], such an increase in density arises from an increase in the degree of network polymerisation induced by γ-irradiation, although the mechanism has not been fully elucidated. Boizot has linked similar effects observed as a result of β-radiation to the migration and clustering of alkali species within the glass [70]. Such changes in network polymerisation would be expected to be apparent in both FTIR and Raman spectra, however, as discussed in Section 4, the FTIR and Raman spectra present no evidence for a change in network polymerisation induced by γ-irradiation, consistent with the invariance in mechanical properties.

4.2. Glass structure variation as detected by Raman and FTIR spectroscopy

Fitting of FTIR and Raman spectra revealed no significant change between the control and γ-irradiated glass samples. Therefore, it can be concluded that γ-irradiation does not induce a significant change in Q speciation in these glasses up to a dose of 8 MGy. Fe has previously been linked to negating the deleterious effect of γ-irradiation [18,61,63], consistent with the mechanical property results, which are determined by the silicate network polymerisation in the glass.

In considering Raman bands associated with Fe^{3+}–S^{2-} bonds in G73 glass, a marked decrease in the 400 cm^{-1} band was observed with increasing dose applied to G73 glass, implying a decrease in the volume fraction of the Fe^{3+}–S^{2-} species. Klimm [58] indicate that this Raman band is uniquely associated with the Fe^{3+}–S^{2-} species. Consequently, this result does not necessarily indicate a decrease in the overall proportion of S^{2-} species, for which there is no evidence from S XES data. This is further supported by the invariant relative intensity of the stretching mode at 990 cm^{-1} band, characteristic of SO_4^{2-} species, which is inconsistent with significant oxidation of S^{2-} species.

4.3. Fe analysis by optical absorption, EPR and Mössbauer spectroscopy

4.3.1. EPR spectroscopy

As shown in Section 3.2.5 no evidence of paramagnetic defects, such as boron oxygen hole centres, were detected by EPR spectroscopy. However, EPR experiments did provide information about Fe^{3+} species in the control glasses, through variation in the intensity ratio of the $g_{eff} \approx 2.0$ and $g_{eff} \approx 4.3$ signals. This variation was attributable to the glass compositions, and is in good agreement with Bingham et al. [31]. However, no significant variation in the intensity ratios in relation to γ-irradiation could be ascertained.

4.3.2. Mössbauer spectroscopy

Fig. 15 shows that there is no significant variation in the overall Fe oxidation state, in response to γ-irradiation, within the estimated errors, in agreement with the study of Eissa et al. [21]. Fig. 21 shows the dipole and quadrupole splitting values for the fits of the Fe^{2+} and Fe^{3+} environments superimposed onto the

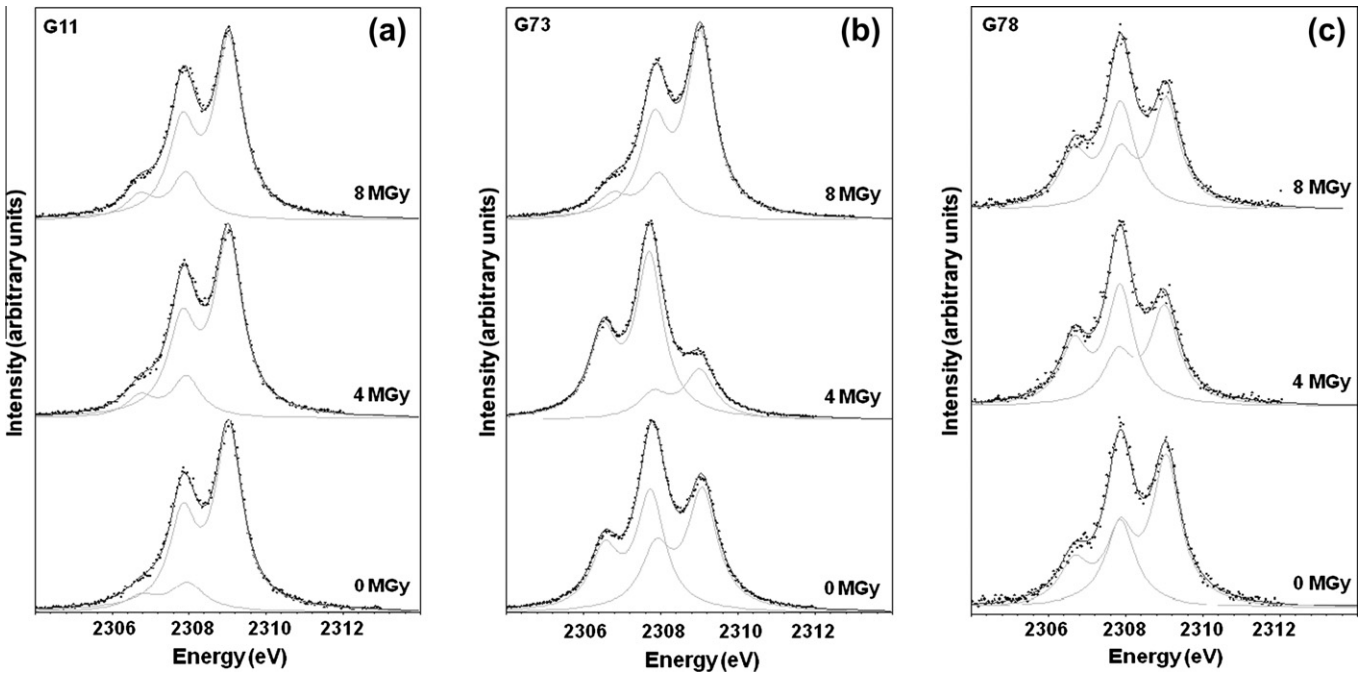

Fig. 19. (a–c) Comparison of XES spectra in control (0 MGy) and γ-irradiated (4 and 8 MGy) samples fitted with Lorentzian line-shapes.

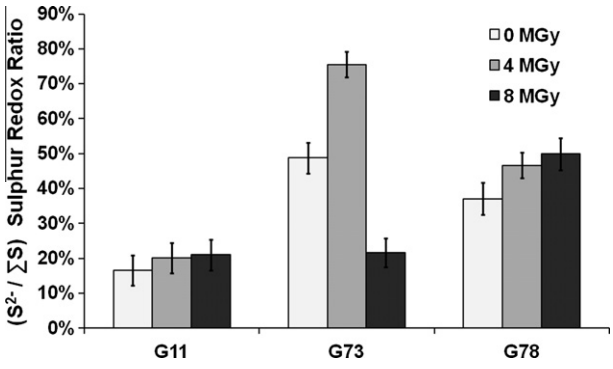

Fig. 20. Comparison of S oxidation state in control (0 MGy) and γ-irradiated (4 and 8 MGy) glasses derived from Lorentzian fitting of XES spectra. Errors bars represent three standard deviations, derived from the fitting of three individual spectra.

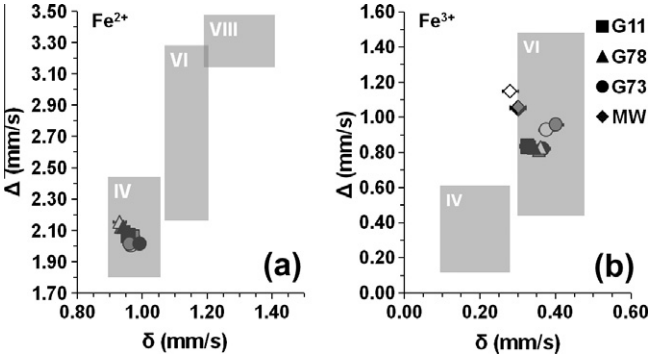

Fig. 21. (a and b) Comparison of Fe dipole (δ) and quadrupole (Δ) splitting in control (0 MGy) and γ-irradiated (4 and 8 MGy) glasses; open, grey and black symbols correspond to dose of 0, 4, and 8 MGy, respectively. Errors bars represent three standard deviations, derived from the fitting of three individual spectra.

speciation plot devised by Dyar [71], highlighting the features associated with the tetrahedral and octahedral coordination environments. In all glasses it is apparent that Fe^{2+} is present in 4-fold coordination sites and Fe^{3+} species are present in 6-fold coordination sites. Fe^{2+} splitting parameters were unaffected by γ-irradiation, however, Fe^{3+} quadrupole splitting results for G73 and MW-25% glasses showed a decrease in quadrupole splitting in proportion to increasing γ-irradiation. This suggests a decrease in the average population of Fe^{3+} in 6-fold coordination in these glasses, and an increased average population of Fe^{3+} in 4-fold coordination.

Overall, the combined mechanical property and spectroscopic data support the mechanism first suggested by Debnath [20] for the remediation of γ-radiation induced defects by the capture of excitons between Fe oxidation states. In this mechanism, effective annihilation of the excitons, i.e. holes and electrons generated by γ irradiation, is achieved by the following redox couple.

$$Fe^{3+} + e^- \rightarrow Fe^{2+}$$
$$Fe^{2+} + h^+ \rightarrow Fe^{3+}$$

Assuming this mechanism to operate in the present study would explain the absence of significant induced changes in glass structure and hence physical properties, preventing the accumulation of radiation induced defects. The mechanism enables the coordination environment of the Fe to undergo a relaxation, for which evidence has been gleaned from the decreased quadrupole splitting observed by Mössbauer spectroscopy, and which has been previously reported [21].

4.3.3. Optical absorption spectroscopy

Optical absorption spectroscopy identified the presence of Fe related absorption bands in all four glasses, including a band associated with Fe^{2+}–O–Fe^{3+} inter-valence interactions. Note that the invariance of these absorption bands and Fe redox determined by Mössbauer spectroscopy cannot provide an explanation for the observed variation in colour in glass G73. However, a correlation between the proportion of S^{2-}, as determined by XES, and the observed variation in colour of G73 glasses was apparent. The Fe^{3+}–S^{2-} species (the amber chromophore) is known to be optically

absorbing at wavelengths of 415 cm^{-1} and provides a possible explanation for the observed colouration [66]. However, further evidence is required to support the presence of this species in the glass G73.

4.4. X-ray absorption and X-ray emission spectroscopy at the SK-edge

The X-ray absorption and X-ray emission experiments conducted on glass G11 showed no significant change in sulphur oxidation within the estimated error. However, glasses G78 and G73 both exhibited a variation in sulphur oxidation state, most strongly in G73. The glass MW-25% was not included in these experiments due to its negligible sulphur content. The changes can be attributed to the capture of electrons and holes generated by the γ-radiation, based on the mechanism that has been proposed by Debnath [20]. The S^{2-}, S^{4+} and S^{6+} oxidation states have been identified in the glasses by the comparison of XANES results to sulphur reference standards, but other sulphur oxidation states may also be present. The variation in sulphur reduction in the glasses can be related to the compositional variations present in the glasses. The Fe content of these three wasteforms decreases in the order G11 > G78 > G73, whereas the sulphur content increases in the order G11 ≈ G78 < G73. Therefore, it is possible that the greater change in sulphur oxidation state observed in G73, and to a lesser extent in G78, are the result of the sulphur being exposed to a higher proportion of γ-radiation derived excitons which would otherwise be annihilated by the more abundant Fe species in glass G11. S could be expected to be preferentially reduced by the γ-radiation induced excitons over Fe as it is known to be more susceptible to chemical reduction, according to the work of Schrieber et al. [72].

The atypical results observed in glass G73 can be explained by the increased incidence of reduced glass components occurring in G73 control sample (0 MGy) in which both S^{2-} and Fe^{2+} are more populous than in the other control samples. This explains the increased extent of sulphur reduction, as the extent of sulphur reduction appears to correlate with the Fe content of the glass. The oxidative step seen at 8 MGy in glass G73, which is atypical of the observations made of the other glasses, provides evidence of two competing processes occurring with regards to sulphur oxidation state in response to γ-irradiation. This may be linked to either the environment in which the samples were irradiated or phase separation occurring at high γ-radiation doses. However, there is insufficient evidence to suggest a likely cause in the reported results, and further work is required.

5. Conclusion

This work has shown that γ-radiation produces no significant change in mechanical properties of the wasteform materials studied, up to 8 MGy, within the precision of the techniques applied. Similarly, γ-irradiation was found to have no significant effect on the glass network as detected through Raman and FTIR spectroscopy, within the precision of the techniques. This has been attributed to the presence of a significant proportion of Fe within the glass compositions, which has been identified providing a mechanism to heal radiation induced defects in glasses of similar compositions [20,62,64]. Mössbauer and EPR spectroscopies provided evidence for a small degree of change in Fe environments within the glasses. This supports the mechanism proposed by Debnath [20], by which excitons produced by the incident γ-radiation are trapped or annihilated by the capture of electrons and holes resulting in oxidation state change in Fe, resulting in no net change in Fe oxidation state, but effecting some change in Fe environment.

Variation in sulphur oxidation state was observed in glasses G73 and G78. This was attributed to γ-radiation induced reduction or oxidation of coordinated sulphur. A dependence on redox state was observed and was most apparent in glass G73. The presence of the Fe^{3+}–S^{2-} species was implied by Raman and optical absorption spectroscopy result in glasses G11, G73 and G78. Raman spectroscopy showed that this species was eliminated by incident γ-radiation in glass G73, which can be connected to the effect of γ-radiation upon S and Fe species within the glass.

These results support past observations of Fe rich alkali-borosilicate exposed to γ-irradiation [16,17,21,64] and parallel observation made in β-radiation experiments [63]. However, the data differs from observations of alkali-borosilicate glasses with low Fe contents, such as Pyrex and the MW-25% base glass, in which a correlation exists between γ-radiation dose and changes of mechanical properties and defect formation [17]. This indicates that the presence of Fe in these glasses, which is present due either to waste loading or for waste compatibility reasons, has a significant and positive effect on the resistance of the wasteform to γ-irradiation. It would be of interest, in future, to investigate this issue in connection with other redox active elements in radioactive waste glasses, such as Mo and Se [73–77]. Finally it may be concluded that γ-radiation does not have a significant deleterious effect on the mechanical stability or composition of simulant inactive UK ILW and HLW glasses, up to the dose of 8 MGy.

Acknowledgements

The authors wish to thank the European Synchrotron Radiation Facility for provisions of synchrotron radiation facilities and ESRF support groups and ID26 beam staff for their assistance, the EPSRC UK National Electron Paramagnetic Resonance Service at The University of Manchester, and Dr. S.D. Forder of Sheffield Hallam University for assistance with ^{57}Fe Mössbauer spectroscopy. N.C. Hyatt is grateful to The Royal Academy of Engineering and the Nuclear Decommissioning Authority for funding. This work was supported in part by an EPSRC Case award co-funded by Magnox Ltd. The authors gratefully acknowledge useful discussion with Paul Health, Dr. Tony Burnett and Dr. Mike James in connection with this research.

References

[1] V.A. Morozov, IAEA Bull. 21 (1979) 17.
[2] N.D. Hutson, C.A. Herman, J.R. Zamecnik, US DOE Report No.WSRC-MS-2000-00884, 2000. <http://sti.srs.gov/fulltext/ms2000884/ms2000884.html>.
[3] C.M. Jantzen, D.K. Peeler, C.A. Cicero, US DOE Report No.WSRC-MS-95-0518, 1995. <http://www.osti.gov/bridge/purl.cover.jsp?purl=/237361VKs8Cg/webviewable/>.
[4] J. Sheng, Glass Technol. Eur. J. Glass Sci. Technol. A 45 (2004) 153.
[5] V. Petitjean, 2002, WM'02 Conf Proc, <http://www.wmsym.org/archives/2002/Proceedings/18/39.pdf>.
[6] I.W. Donald, B.L. Metcalfe, N.J. Taylor, J. Mater. Sci. 32 (1997) 5851.
[7] M.I. Ojovan, W.E. Lee, An Introduction to Nuclear Waste Immobilisation, Elsevier, Amsterdam, 2005.
[8] W.E. Lee, M.I. Ojovan, M.C. Stennett, N.C. Hyatt, Adv. Appl. Ceram. 105 (3) (2006).
[9] W.J. Weber, Nucl. Instrum. Meth. Phys. Res. B 32 (1998) 471.
[10] W.J. Weber, R.C. Ewing, C.A. Angell, G.W. Arnold, A.N. Cormack, J.M. Delaye, D.L. Griscom, J. Mater. Res. 12 (1997) 946.
[11] R.C. Ewing, W.J. Weber, F.W. Clinard Jr, Prog. Nucl. Eng. 29 (1995) 63.
[12] K. Sun, L.M. Wang, R.C. Ewing, W.J. Weber, Nucl. Instrum. Meth. Phys. Res. B 218 (2004) 368.
[13] E. Malchukova, B. Boizot, G. Petite, D. Ghaleb, Eur. Phys. J. Appl. Phys. 45 (2009) 10701.
[14] T. Mizutani, J. Non-Cryst. Solid 181 (1995) 123.
[15] H. Hosono, N. Matsunami, Nucl. Instrum. Meth. Phys. Res. B 141 (1998) 566.
[16] G. Brown, J. Mater. Sci. 10 (1975) 1841.
[17] G. Brown, J. Mater. Sci. 10 (1975) 1481.
[18] E.A. Vanina, M.A. Chibisova, S.M. Sokolova, Glass Ceram. 63 (2006) 11.
[19] W.A. Zdaniewski, T.E. Easler, R.C. Bradt, J. Am. Ceram. Soc. 66 (1983) 311.
[20] R. Debnath, J. Mater. Res. 16 (2001) 127.
[21] N.A. Eissa, N.H. Sheta, W.M. El-Meligy, S.M. El-Minyawi, H.A. Sallam, Radiat. Phys. Chem. 44 (1994) 35.
[22] J.A.C. Marples, Glass Technol. 29 (1988) 230.

[23] P.A. Bingham, N.C. Hyatt, R.J. Hand, C.R. Wilding, Sci. Basis Nucl. Waste Manage. XXXII Mater. Res. Soc. Symp. Proc. 1124 (2009) 161.
[24] P.A. Bingham, A.J. Connelly, R.J. Hand, N.C. Hyatt, Nucl. Future 6 (2010) 250.
[25] W.R. Davis, Trans. Brit. Ceram. Soc. 67 (1968) 515.
[26] H. Matzke, E. Toscano, J. Am. Ceram. Soc. 69 (1986) C138.
[27] J. Shelby, J. Appl. Phys. 51 (1980) 2561.
[28] A.J. Connelly, R. Hand, P.A. Bingham, N.C. Hyatt, J. Nucl. Mater. 408 (2011) 188.
[29] M. Kavčič, A. Karydas, Ch. Zarkadas, Nucl. Instr. Meth. B 222 (2004) 601.
[30] M. Žitnik, M. Kavčič, K. Bučar, A. Mihelič, Nucl. Instrum. Meth. B 267 (2009) 221.
[31] P.A. Bingham, J.M. Parker, T. Searle, J.M. Williams, I. Smith, CR Chim. 5 (2002) 787.
[32] P.A. Bingham, J.M. Parker, T. Searle, J.M. Williams, K. Fyles, J. Non-Cryst. Solids 253 (1999) 203.
[33] P.A. Bingham, C.M. Jackson, J. Archaeol. Sci. 35 (2008) 302.
[34] C.R. Bamford, Colour Generation and Control in Glass, Glass Science and Technology, vol. 2, Elsevier, Amsterdam, 1977.
[35] P. Piscilella, M. Pelino, J. Eur. Ceram. Soc. 25 (2005) 1855.
[36] F.H. El-Batal, E.M. Khalil, Y.M. Hamdy, H.M. Zidan, H.S. Aziz, A.M. Abdelghany, Silicon 2 (2010) 41.
[37] Y.K. Lee, Y.L. Peng, M. Tomozawa, J. Non-Cryst. Solids 222 (1997) 125.
[38] M. Toderas, S. Filip, I. Ardelean, J. Optoelectron. Adv. Mater. 8 (2006) 1121.
[39] J. Kaewkhao, W. Siriprom, S. Insiripong, T. Ratana, T. Ratana, C. Kedkaew, P. Limsuwan, J. Phys.: Conf. Ser. 266 (2011) 012012.
[40] H. Darwish, M, M. Gomaa, J. Mater. Sci.: Mater. Electron. 17 (2006) 35.
[41] S.A. MacDonald, C.R. Schardt, D.J. Masiello, J.H. Simmons, J. Non-Cryst. Solids 275 (2000) 72.
[42] P.L. King, C.D.M. Dufresne, K.N. Dalby, Lunar Planet. Sci. XXXIX (2008) 2256.
[43] C.P. Kaushik, R.K. Mishra, P. Sengupta, A. Kumar, D. Das, G.B. Kale, K. Raj, J. Nucl. Mater. 358 (2006) 129.
[44] A.A. Ahmed, N.A. Sharaf, R.A. Condrate, J. Non-Cryst. Solids 210 (1997) 59.
[45] K. Baert, W. Meulebroeck, H. Wouters, P. Cosyns, K. Nys, H. Thienpont, H. Terryn, J. Raman. Spectrosc. 42 (2011) 1789.
[46] T. Tsujimura, X. Xue, M. Kanzaki, Geochim. Cosmochim. Acta 68 (2004) 5081.
[47] M. Lenoir, D.R. Neuville, M. Malki, A. Grandjean, J. Non-Cryst. Solids 356 (2010) 2722.
[48] K.T. Winther, E.B. Watson, G.B. Korenowski, Am. Mineral. 83 (1998) 1141.
[49] D.A. McKeown, A.C. Buechele, C. Viragh, I. Pegg, J. Nucl. Mater. 399 (2010) 13.
[50] P. McMillan, Am. Mineral. 69 (1984) 622.
[51] C. Jegou, R. Caraballo, J. De Bonfils, V. Broudic, S. Peuget, T. Vercouter, D. Roudil, J. Nucl. Mater. 399 (2010) 68.
[52] M. Mercier, A. Di Muro, D. Giordano, N. Metrich, P. Lesne, M. Pichavant, B. Scaillet, R. Clocchiatti, G. Montgnac, Geochim. Cosmochim. Acta 73 (2009) 197.
[53] V. Magnien, D.R. Neuville, L. Cormier, J. Roux, J.L. Hazelmann, O. Pinet, P. Richet, J. Nucl. Mater. 356 (2006) 190.
[54] A. Di Muro, N. Metrich, M. Mercier, D. Giordano, D. Massare, G. Montagnac, Chem. Geol. 259 (2009) 78.
[55] B.G. Parkinson, D. Holland, M.E. Smith, C. Larson, J. Doerr, M. Affatigato, S.A. Feller, A.P. Howes, C.R. Scales, J. Non-Cryst. Solids 354 (2008) 1936.
[56] V. Magnien, D. Neuville, L. Cormier, J. Roux, J. Hazemann, D. De Ligny, S. Pascarelli, I. Vickridge, O. Pinet, P. Richet, Geochim. Cosmochim. Acta 72 (2008) 2157.
[57] M. Lenoir, A. Grandjean, S. Poissonnet, D.R. Neuville, J. Non-Cryst. Solids 355 (2009) 1468.
[58] K. Klimm, Am. Mineral. 95 (2010) 1574.
[59] S.N. White, Chem. Geol. 259 (2009) 240.
[60] G.A. Hope, R. Woods, C.G. Munce, Miner. Eng. 14 (2001) 1565.
[61] D.W. Bishop, P.S. Thomas, A.S. Ray, Mater. Res. Bull. 35 (2000) 1123.
[62] R. Cases, D.L. Griscom, Nucl. Instrum. Meth. Phys. Res. B 1 (1984) 503.
[63] F.Y. Olivier, B. Boizot, D. Ghaleb, G. Petite, J. Non-Cryst. Solids 351 (2005) 1061.
[64] D.L. Griscom, C.I. Merzbacher, R.A. Weeks, R.A. Zuhr, J. Non-Cryst. Solids 258 (1999) 34.
[65] E.J. Friebele, L.K. Wilson, A.W. Dozier, D.L. Kinser, Phys. Status Solidi (B) 45 (1971) 323.
[66] P.A. Bingham, A.J. Connelly, R.J. Hand, N.C. Hyatt, P.A. Northrup, R. Alonso Mori, P. Glatzel, M. Kavčič, K. Bučar, R. Edge, Glass Technol. Eur. J. Glass Sci. Technol. A 51 (2010) 63.
[67] D.L. Griscom, J. Non-Cryst. Solids 67 (1984) 81.
[68] E.A. Zhilinskaya, V.N. Lazukin, E.A. Bychkov, I.L. Likholit, J. Non-Cryst. Solids 119 (1990) 263.
[69] L. Backnaes, J. Stelling, H. Behrens, J. Goettlicher, S. Mangold, O. Verheijen, R.G.C. Beerkens, J. Deubener, J. Am. Ceram. Soc. 91 (2008) 721.
[70] B. Boizot, N. Ollier, F. Olivier, G. Petite, D. Ghaleb, E. Makchukova, Nucl. Instrum. Meth. Phys. Res. B 240 (2005) 146.
[71] M. Darby Dyar, D.G. Agresti, M.W. Schaefer, C.A. Grant, E.C. Sklute, Ann. Rev. Earth Planet. Sci. 34 (2006) 83.
[72] H.D. Schrieber, R.W. Fowler, C.C. Ward, Phys. Chem. Glasses 34 (1993) 66.
[73] P.A. Bingham, A.J. Connelly, N.J. Cassingham, J. Non-Cryst. Solids 357 (2011) 2726.
[74] R.J. Hand, R.J. Short, S. Morgan, N.C. Hyatt, G. Moebus, W.E. Lee, Glass Technol. 46 (2005) 121.
[75] R.J. Short, R.J. Hand, N.C. Hyatt, G. Mobus, J. Nucl. Mater. 340 (2005) 179.
[76] R.J. Short, R.J. Hand, N.C. Hyatt, Mater. Res. Symp. Proc. 757 (2003) 141.
[77] R.J. Short, R.J. Hand, N.C. Hyatt, Mater. Res. Symp. Proc. 807 (2004) 169.